Dynamics of spin-nematic bright solitary waves in spin-tensor-momentum coupled Bose-Einstein condensates

Xu Qiu,[1] Ai-Yuan Hu,[1] Yongyong Cai,[2] Hiroki Saito,[3] Xiao-Fei Zhang,[4,*] and Lin Wen[1,†]

[1]*College of Physics and Electronic Engineering, Chongqing Normal University, Chongqing 401331, China*

[2]*Laboratory of Mathematics and Complex Systems and School of Mathematical Sciences, Beijing Normal University, Beijing 100875, China*

[3]*Department of Engineering Science, University of Electro-Communications, Tokyo 182-8585, Japan*

[4]*Department of Physics, Shaanxi University of Science and Technology, Xi'an 710021, China*

(Received 25 September 2022; accepted 2 March 2023; published 9 March 2023)

We explore the dynamics of bright solitary waves in one-dimensional spin-tensor-momentum coupled spin-1 Bose-Einstein condensates. Our results show that the solitary waves have nonzero spin and nematicity simultaneously, hence we call them spin-nematic solitary waves. The ground-state solitary waves carry a finite momentum and display the zero-energy modes arising from symmetry breaking. In the motion of the solitary wave, the spin-tensor-momentum coupling induces the flip of the spin-nematic vector on a unit Bloch sphere, which in turn produces a force to result in the oscillatory motion of the solitary wave. The effects of a harmonic trap are also analyzed. These findings reveal the unique properties of solitary waves affected by the spin-tensor-momentum coupling.

DOI: 10.1103/PhysRevA.107.033308

I. INTRODUCTION

By using atom-light coupling, various artificial gauge potentials can be realized in ultracold neutral atoms [1], allowing one to explore a panoply of novel phenomena at the quantum level. An important application is to couple the hyperfine spins with orbital degrees of freedom and synthesize the spin-orbit coupling (SOC), such as the spin-linear-momentum coupling [2–8] and the spin-orbital-angular-momentum coupling [9–11]. Since the SOC significantly modifies the single-particle dispersion and leads to degeneracy at a finite momentum or angular momentum, a variety of nontrivial few- and many-body quantum phenomena have been successively predicted theoretically and realized experimentally in Bose-Einstein condensates (BEC) and degenerate Fermi gases, such as a supersolid stripe phase [12–16], unconventional Fermi superfluids [17–20], and diverse exotic vortex states with nontrivial topological spin textures [21–26].

As it is known, the nonlinear atomic interaction gives rise to the solitary wave in ultracold atoms [27–40], which has important potential applications in coherent atom optics, atom interferometry, and atom transport. In particular, if two colliding solitary waves pass through each other without losing their identity, such solitary waves are often termed solitons to suggest the particlelike property [41]. In the past decade, the realization of SOC in ultracold atoms has drawn enormous research interest to explore novel solitary wave structures and interesting dynamical behaviors of solitary waves, and a variety of solitary wave species have been predicted in Bose and Fermi gases with SOC, such as the stripe soliton, the two-dimensional composite soliton, and the half-vortex gap soliton in BEC [42–65], as well as the dark soliton with Majorana zero modes in Fermi gases [66–69]. Therefore, the ultracold atoms with SOC provide a new platform to study the novel dynamics of solitary waves inside a gauge field.

Very recently, the spin-tensor-momentum coupling (STMC) has also been realized experimentally in ultracold three-component Fermi gases [70], and a theoretical scheme for realizing the STMC in Bose gases has also been proposed [71]. The STMC is a new type of SOC, where the momentum couples with the rank-2 spin-quadrupole tensor, rather than with the rank-1 spin vector in spin-linear-momentum coupling, and thus it can generate different single-particle band structures and nontrivial quantum phenomena in the presence of atomic interaction. In a BEC, it has been demonstrated that the STMC can generate a new type of dynamical stripe state with a widely tunable period and high visibility, paving the way for the direct experimental observation of the supersolidlike state [71]. In an optical lattice, the STMC induces different types of topological triply degenerate points connected by intriguing Fermi arcs at surfaces [72], which may give rise to novel quasiparticles and nontrivial topological matter. In the aspects of solitary waves, due to the different symmetries of the STMC from the usual SOC, the stationary solitary waves would also display different profiles [73].

In this paper, we reveal the interesting dynamical features of spin-nematic bright solitary waves in BEC with STMC, which have nonzero spin and nematicity simultaneously. By performing the variational analysis, we first derive the equations of motion for the variational parameters of the solitary waves, including the center-of-mass coordinate, momentum, amplitude, and relative phase. Our analytical and numerical results show that the ground-state solitary waves have a finite

*xfzhang_physics@163.com
†wlqx@cqnu.edu.cn

momentum, and Goldstone modes and oscillation modes have been identified in its low-energy excitation spectrum. The dynamical properties of solitary waves have also been studied, which display that, under the action of the STMC and the Raman coupling, the spin-nematic vector of the solitary wave will flip on a unit Bloch sphere, which in turn couples to the center-of-mass momentum and produces a force to affect the orbital motion of the solitary wave, leading to unique dynamical behaviors. In the presence of a harmonic trap, it competes with the spin-dependent interaction in determining the center of mass of the ground-state solitary wave, and it induces an additional collective oscillation with frequency related to the trapping frequency. These findings suggest a new scenario for manipulating the dynamics of solitary waves in BEC.

The remainder of the present paper is organized as follows. In Sec. II, we formulate the theoretical model describing the dynamics of a spin-1 BEC with STMC. By using the hyperbolic secant function as an ansatz for the bright solitary wave, we derive the equations of motion for the variational parameters in Sec. III. For the uniform system without trap, the dynamics of solitary waves without and with spin-dependent interaction are investigated analytically and numerically in Secs. IV and V, respectively. The effects of a harmonic trap on the dynamics of solitary waves are discussed in Sec. VI. Finally, we summarize the main results of the present paper in Sec. VII.

II. MODEL

We consider a BEC comprised of three hyperfine states of spin-1 atoms with mass m, such as ^{87}Rb and ^{23}Na. The three hyperfine states are denoted by $|\uparrow\rangle$, $|0\rangle$, and $|\downarrow\rangle$, respectively. The STMC can be created by using three Raman laser beams with a wave vector k_r to couple these three states, where the two laser beams propagate in the z direction, and the third laser beam propagates in the $-z$ direction [70,71]. These three laser beams induce Raman transitions between the hyperfine states $|0\rangle$ and $|\uparrow(\downarrow)\rangle$, in which the atoms can be flipped from $|0\rangle$ to $|\uparrow(\downarrow)\rangle$ states and simultaneously imparted momentum $2\hbar k_r$ via the two-photon Raman process. Therefore, the effective single-particle Hamiltonian is given by [70,71]

$$\hat{H}_0 = \begin{pmatrix} \frac{\hat{\mathbf{p}}^2}{2m} + \delta_r & -\frac{\Omega_r}{2} e^{-i2k_r z} & 0 \\ -\frac{\Omega_r}{2} e^{i2k_r z} & \frac{\hat{\mathbf{p}}^2}{2m} & -\frac{\Omega_r}{2} e^{i2k_r z} \\ 0 & -\frac{\Omega_r}{2} e^{-i2k_r z} & \frac{\hat{\mathbf{p}}^2}{2m} + \delta_r \end{pmatrix}, \tag{1}$$

where $\hat{\mathbf{p}}^2 = \hat{p}_x^2 + \hat{p}_y^2 + \hat{p}_z^2$, and $\hat{p}_\nu = -i\hbar\partial_\nu$ with $\nu = x, y$, and z is the momentum operator. δ_r and Ω_r are the two-photon Raman detuning and Raman coupling strength, respectively. Within the mean-field theory at zero temperature, the energy functional in the presence of atomic interactions is

$$E = \int d^3\mathbf{r} \Big[\Phi^\dagger \hat{H}_0 \Phi + \frac{G_n}{2} (\Phi^\dagger \Phi)^2 + \frac{G_s}{2} (|\Phi_\uparrow|^2 - |\Phi_\downarrow|^2)^2 + G_s |\Phi_\uparrow^* \Phi_0 + \Phi_0^* \Phi_\downarrow|^2 \Big], \tag{2}$$

where the wave function $\Phi = (\Phi_\uparrow, \Phi_0, \Phi_\downarrow)^T$, with T being the transpose, satisfies the normalization condition $\int \Phi^\dagger \Phi d^3\mathbf{r} = 1$, and the superscripts $*$ and $\dagger$ represent the conjugate and the conjugate transpose, respectively. The coefficients $G_n = 4\pi\hbar^2 N(a_0 + 2a_2)/(3m)$ and $G_s = 4\pi\hbar^2 N(a_2 - a_0)/(3m)$ in the the nonlinear terms are the strengths of the spin-independent and spin-dependent interactions, respectively, where N is the total particle number, and a_0 and a_2 are the s-wave scattering lengths of total spin-0 and spin-2 channels, respectively.

In the single-particle Hamiltonian (1), the off-diagonal terms show clearly the spin-flipping process and the momentum transfer. To illustrate the connection with the STMC effect, we make the unitary transformations $\Phi_\uparrow = e^{-i2k_r z}\tilde{\Phi}_\uparrow$, $\Phi_0 = \tilde{\Phi}_0$, and $\Phi_\downarrow = e^{-i2k_r z}\tilde{\Phi}_\downarrow$, and then the single-particle Hamiltonian (1) becomes

$$\hat{H}_0' = \frac{\hat{\mathbf{p}}^2}{2m} + \left(\delta_r + 4E_r - \frac{4E_r}{\hbar k_r}\hat{p}_z\right) F_z^2 - \frac{\Omega_r}{\sqrt{2}} F_x, \tag{3}$$

where $E_r = \hbar^2 k_r^2/2m$ is the recoil energy, and F_ν's with $\nu = x$, y, and z are the spin-1 matrices

$$F_x = \frac{1}{\sqrt{2}} \begin{pmatrix} 0 & 1 & 0 \\ 1 & 0 & 1 \\ 0 & 1 & 0 \end{pmatrix}, \; F_y = \frac{i}{\sqrt{2}} \begin{pmatrix} 0 & -1 & 0 \\ 1 & 0 & -1 \\ 0 & 1 & 0 \end{pmatrix}, \; F_z = \begin{pmatrix} 1 & 0 & 0 \\ 0 & 0 & 0 \\ 0 & 0 & -1 \end{pmatrix}. \tag{4}$$

The term $\propto \hat{p}_z F_z^2$ in the Hamiltonian (3) is the so-called STMC, which couples the atomic momentum $\hat{p}_z$ with the rank-2 symmetric spin-nematic tensor $N_{zz} = F_z^2$.

After the unitary transformation, the energy functional (2) becomes

$$E = \int d^3\mathbf{r} \Big[\tilde{\Phi}^\dagger \hat{H}_0' \tilde{\Phi} + \frac{G_n}{2} (\tilde{\Phi}^\dagger \tilde{\Phi})^2 + \frac{G_s}{2} (|\tilde{\Phi}_\uparrow|^2 - |\tilde{\Phi}_\downarrow|^2)^2 + G_s |e^{i2k_r z} \tilde{\Phi}_\uparrow^* \tilde{\Phi}_0 + e^{-i2k_r z} \tilde{\Phi}_0^* \tilde{\Phi}_\downarrow|^2 \Big], \tag{5}$$

where $\tilde{\Phi} = (\tilde{\Phi}_\uparrow, \tilde{\Phi}_0, \tilde{\Phi}_\downarrow)^T$. The energy functional (5) shows that the unitary transformation introduces the additional exponential factors $e^{i2k_r z}$ and $e^{-i2k_r z}$ into the spin-dependent interaction terms. If the spin-dependent interaction vanishes (i.e., $G_s = 0$), the energy functional (5) does not contain the spatial coordinate explicitly, and thus the system has translational symmetry. In the presence of the spin-dependent interaction, the spatial-dependent exponential factors break the translational symmetry. In this paper we perform the study in the unitary transformed frame, which can make the STMC effect more transparent.

By using $i\hbar\partial\tilde{\Phi}_\sigma/\partial t = \delta E/\delta\tilde{\Phi}_\sigma^*$, we can obtain the time-dependent Gross-Pitaevskii (GP) equation, which describes the dynamics of the BEC. We assume that the BEC is confined in a harmonic trap $V(\mathbf{r}) = \frac{1}{2}m[\omega_\perp^2(x^2 + y^2) + \omega_z^2 z^2]$ with frequencies $\omega_\perp \gg \omega_z$, and the motional degrees of freedom of atoms in the xy plane are frozen into the ground state of the harmonic-oscillator potential. The dynamics of such a cigar-shaped BEC can be considered to be effectively one-dimensional along the z direction. By using $\omega_\perp^{-1}$ and

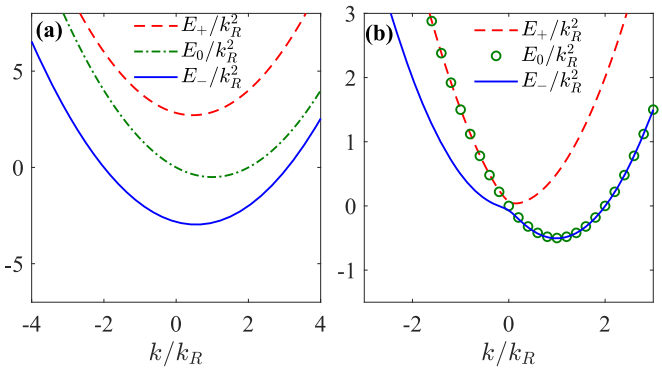

FIG. 1. Single-particle energy-band structures in the momentum space. (a) $\Omega_R/k_R^2 = 4$. (b) $\Omega_R/k_R^2 = 0.1$.

$\xi_\perp = \sqrt{\hbar/m\omega_\perp}$ as the units of time and length, the dimensionless GP equation in quasi-one dimension is given by

$$i\frac{\partial\psi_\uparrow}{\partial t} = -\frac{1}{2}\frac{\partial^2\psi_\uparrow}{\partial z^2} + ik_R\frac{\partial\psi_\uparrow}{\partial z} + \frac{1}{2}\gamma^2 z^2\psi_\uparrow - \frac{\Omega_R}{2}\psi_0 + g_n\rho\psi_\uparrow + g_s(\rho_\uparrow + \rho_0 - \rho_\downarrow)\psi_\uparrow + g_s e^{i2k_R z}\psi_0^2\psi_\downarrow^*, \tag{6a}$$

$$i\frac{\partial\psi_0}{\partial t} = -\frac{1}{2}\frac{\partial^2\psi_0}{\partial z^2} + \frac{1}{2}\gamma^2 z^2\psi_0 - \frac{\Omega_R}{2}(\psi_\uparrow + \psi_\downarrow) + g_n\rho\psi_0 + g_s(\rho_\uparrow + \rho_\downarrow)\psi_0 + 2g_s e^{-i2k_R z}\psi_\uparrow\psi_0^*\psi_\downarrow, \tag{6b}$$

$$i\frac{\partial\psi_\downarrow}{\partial t} = -\frac{1}{2}\frac{\partial^2\psi_\downarrow}{\partial z^2} + ik_R\frac{\partial\psi_\downarrow}{\partial z} + \frac{1}{2}\gamma^2 z^2\psi_\downarrow - \frac{\Omega_R}{2}\psi_0 + g_n\rho\psi_\downarrow + g_s(\rho_\downarrow + \rho_0 - \rho_\uparrow)\psi_\downarrow + g_s e^{i2k_R z}\psi_\uparrow^*\psi_0^2, \tag{6c}$$

where we have taken $\delta_r = -4E_r$ for the sake of simplicity, which does not affect the essential physics qualitatively. In the GP equation (6), the wave function $\psi_\sigma(z,t)$ satisfies the normalization condition $\sum_\sigma \int_{-\infty}^{+\infty} |\psi_\sigma|^2 dz = 1$, with $\sigma = \uparrow$, 0, and $\downarrow$. We define the total density $\rho = \sum_\sigma \rho_\sigma$ with $\rho_\sigma = |\psi_\sigma|^2$, and $k_R = 2k_r\xi_\perp$ and $\Omega_R = \Omega_r/\hbar\omega_\perp$ are the dimensionless strengths of the STMC and the Raman coupling, respectively. The parameter $\gamma = \omega_z/\omega_\perp \ll 1$ is the aspect ratio of the trap, and $g_n = 2N(a_0 + 2a_2)/(3\xi_\perp)$ and $g_s = 2N(a_2 - a_0)/(3\xi_\perp)$ are the dimensionless strengths of the spin-independent and spin-dependent interactions. Since we are interested in bright solitary waves in this paper, we always assume $g_n < 0$, which may be realized by the Feshbach resonance technique. We also assume that g_s can be either positive or negative with $|g_s| \ll |g_n|$.

For the uniform system without trap, the single-particle energy spectra for $\delta_r = -4E_r$ in the momentum space are

$$E_\pm = \frac{1}{2}k^2 - \frac{1}{2}k_R k \pm \frac{1}{2}\sqrt{k_R^2 k^2 + 2\Omega_R^2}, \tag{7a}$$

$$E_0 = \tfrac{1}{2}k^2 - k_R k, \tag{7b}$$

where k denotes the dimensionless momentum. Figure 1 shows the single-particle energy band structures in the momentum space. The bottom energy band E_- only has a single global minimum at a finite momentum, which is related to k_R and Ω_R. When Ω_R/k_R^2 is small, as shown in Fig. 1(b), the middle energy band E_0 is close to the left and right sides of E_+ and E_-, respectively. In particular, similarly to the spin-linear-momentum coupled BEC [43], there is a semi-infinite gap below the minimum of the bottom energy band E_-, where the plane wave or linear mode propagations are forbidden, but the bright solitary waves induced by the attractive spin-independent atomic interaction can exist in this semi-infinite gap.

The spinor BEC with spin $F \geqslant 1$ can exhibit both magnetism and nematicity [74–77], which are described by the spin vector $S_\nu = \int \Psi^\dagger F_\nu \Psi dz$ and the nematic tensor $\mathcal{N}_{\nu\nu'} = \int \Psi^\dagger N_{\nu\nu'}\Psi dz$, with $\Psi = (\psi_\uparrow, \psi_0, \psi_\downarrow)^T$, respectively, where $N_{\nu\nu'} = \frac{1}{2}(F_\nu F_{\nu'} + F_{\nu'}F_\nu) - \frac{2}{3}\delta_{\nu\nu'}$ is the symmetrized SU(3) nematic tensor. In general, the 3×3 nematic matrix $\mathcal{N}$ composed of $\mathcal{N}_{\nu\nu'}$ have three eigenvalues denoted as $\lambda_{1,2,3}$, which characterize the alignment axis of nematicity and distinguish different nematic states. For example, the BEC in the uniaxial nematic state has $\lambda_1 \neq \lambda_2 = \lambda_3$, and the biaxial nematic state has $\lambda_1 \neq \lambda_2 \neq \lambda_3$ [74–77]. We use the spin vector and the nematic tensor to depict the features of solitary waves, which are useful for clarifying the underlying physical mechanism behind the dynamics of solitary waves.

We use the Bogoliubov approach to study the dynamical stabilities and low-energy excitations of the stationary solitary waves. We decompose the wave function $\psi_\sigma(z,t)$ into the stationary state $\psi_{\sigma,0}(z)$ and the fluctuation $\delta\psi_\sigma(z,t)$, that is, $\psi_\sigma(z,t) = e^{-i\mu t}[\psi_{\sigma,0}(z) + \delta\psi_\sigma]$, with $\delta\psi_\sigma = u_\sigma(z)e^{-i\omega t} - v_\sigma^*(z)e^{i\omega^* t}$, where ω is the excitation frequency taken as a complex number, μ is the chemical potential, and $u_\sigma(z)$ and $v_\sigma(z)$ are the wave functions of the Bogoliubov quasiparticle excitations. These functions satisfy the Bogoliubov–de Gennes (BdG) equation

$$\begin{pmatrix} A & B \\ -B^* & -A^* \end{pmatrix}\begin{pmatrix} U \\ V \end{pmatrix} = \omega\begin{pmatrix} U \\ V \end{pmatrix}, \tag{8}$$

where $U = (u_\uparrow, u_0, u_\downarrow)^T$ and $V = (v_\uparrow, v_0, v_\downarrow)^T$. The details of A and B are given in the Appendix. The Bogoliubov excitation frequency ω can be numerically obtained by diagonalizing the BdG equation [78]. The stationary solitary wave is dynamically stable under a perturbation, if ω is real; otherwise it is unstable.

III. VARIATIONAL ANALYSIS

For the uniform system without trap ($\gamma = 0$), the GP equation (6) has two special exact uniaxial nematic solitary wave solutions with $\lambda_1 = -\frac{2}{3}$ and $\lambda_2 = \lambda_3 = \frac{1}{3}$, which are called the polar states with $S_\nu = 0$. One is $\psi_0 = 0$ and $\psi_\uparrow = -\psi_\downarrow = \sqrt{\frac{\eta}{4}}\mathrm{sech}\{\eta[z - (k - k_R)t]\}e^{ikz}$ with $\eta = -g_n/2$ and the momentum k, and the GP equation (6) reduces to the two-component Manakov equations satisfied by $\psi_\uparrow$ and $\psi_\downarrow$. In this state, the STMC only contributes to the velocity of the solitary wave, which moves the solitary wave at a constant velocity even for $k = 0$, but the Raman coupling does not affect the dynamics of solitary waves. The other solution is $\psi_\uparrow = \psi_\downarrow = 0$ and $\psi_0 = \sqrt{\frac{\eta}{2}}\mathrm{sech}[\eta(z - kt)]e^{ikz}$, with $\eta = -g_n/2$, where the GP equation (6) reduces to the single nonlinear Schrödinger equation satisfied by ψ_0, and the solitary wave is independent of the STMC and the Raman coupling. However, for the general case with $\psi_\sigma \neq 0$, it is difficult to construct the exact

solitary wave solutions of the GP equation (6) analytically even without the trap. Therefore, we use the variational approach to perform the analytical study [79].

One can observe that the GP equation (6) has the exchange symmetry with $\psi_\uparrow \leftrightarrow \psi_\downarrow$, which means $\psi_\uparrow = \psi_\downarrow e^{i\phi}$, with ϕ being an arbitrary time-independent constant. On the other hand, the STMC results in the atoms condensing around a single nonzero momentum, and the solitary waves carry a finite momentum k. Thus, we take the following variational wave functions to describe the bright solitary waves:

$$\begin{pmatrix}\psi_\uparrow\\ \psi_0\\ \psi_\downarrow\end{pmatrix} = \sqrt{\frac{\eta}{2}}\begin{pmatrix}\frac{1}{\sqrt{2}}\sin(\theta)e^{i\phi_\uparrow}\\ \cos(\theta)e^{i\phi_0}\\ \frac{1}{\sqrt{2}}\sin(\theta)e^{i\phi_\downarrow}\end{pmatrix}\mathrm{sech}[\eta(z-z_c)]e^{ikz}, \tag{9}$$

where we assume that the solitary waves in three components have the same width η^{-1} and center-of-mass coordinate z_c for the sake of simplicity. The parameters θ and ϕ_σ with $\sigma = \uparrow, 0$, and $\downarrow$ are related to the amplitude and the phase of the solitary wave, respectively. All the variational parameters are time dependent. As we see below, although the variational wave functions are relatively simple and have quantitative differences from the numerical solutions of the GP equation in some parameter regimes, they can still extract the essential physics and provide the qualitative explanations of the dynamics of solitary waves.

The Lagrangian of the system is

$$\begin{aligned}\mathcal{L} = \int_{-\infty}^{+\infty}\Bigg[&\frac{i}{2}\sum_\sigma\left(\psi_\sigma^*\frac{\partial\psi_\sigma}{\partial t} - \psi_\sigma\frac{\partial\psi_\sigma^*}{\partial t}\right) + \frac{1}{2}\Psi^\dagger\left(\frac{\partial^2}{\partial z^2} - \gamma^2 z^2\right)\Psi\\ &-\Psi^\dagger\left(ik_R F_z^2\frac{\partial}{\partial z} - \frac{\Omega_R}{\sqrt{2}}F_x\right)\Psi - \frac{g_n}{2}\rho^2 - \frac{g_s}{2}(\rho_\uparrow - \rho_\downarrow)^2\\ &-g_s\left|e^{ik_R z}\psi_\uparrow^*\psi_0 + e^{-ik_R z}\psi_0^*\psi_\downarrow\right|^2\Bigg]dz.\end{aligned} \tag{10}$$

Inserting Eq. (9) into the Lagrangian, we can get

$$\mathcal{L} = -z_c\frac{dk}{dt} - \frac{1}{2}\sin^2(\theta)\frac{d(\phi_\uparrow + \phi_\downarrow)}{dt} - \cos^2(\theta)\frac{d\phi_0}{dt} - E, \tag{11}$$

with the mean-field energy

$$\begin{aligned}E = &\frac{1}{2}k^2 - k_R k\sin^2(\theta) + \frac{1}{6}\eta^2 + \frac{1}{12}\eta[2g_n + g_s\sin^2(2\theta)]\\ &-\frac{\sqrt{2}}{2}\Omega_R\sin(2\theta)\cos\left(\frac{\Phi}{2}\right)\cos\left(\frac{\phi_\uparrow - \phi_\downarrow}{2}\right) + \frac{1}{2}\gamma^2 z_c^2\\ &+\frac{\pi^2\gamma^2}{24\eta^2} + \frac{1}{12}\pi g_s\eta f(\eta)\sin^2(2\theta)\cos(\Theta),\end{aligned} \tag{12}$$

where $\Theta = 2k_R z_c - \Phi$, with $\Phi = \phi_\uparrow + \phi_\downarrow - 2\phi_0$, and the function $f(\eta) = k_R(k_R^2/\eta^2 + 1)\mathrm{csch}(k_R\pi/\eta)/\eta$ is positive regardless of k_R/η. Using the Euler-Lagrange equation $\frac{\partial\mathcal{L}}{\partial\zeta} - \frac{d}{dt}(\frac{\partial\mathcal{L}}{\partial\dot{\zeta}}) = 0$, with $\dot{\zeta} = d\zeta/dt$ (ζ represents a variational parameter), we obtain the equations of motion for the variational parameters:

$$\frac{dk}{dt} = \frac{1}{6}\pi k_R g_s\eta f(\eta)\sin^2(2\theta)\sin(\Theta) - \gamma^2 z_c, \tag{13a}$$

$$\frac{1}{3}\eta = \frac{\pi^2\gamma^2}{12\eta^3} - \frac{1}{6}g_n - \frac{1}{12}g_s\sin^2(2\theta) - \frac{1}{12}\pi g_s\sin^2(2\theta)\cos(\Theta)\left[f(\eta) + \eta\frac{df}{d\eta}\right], \tag{13b}$$

$$\frac{dz_c}{dt} = k - k_R\sin^2(\theta), \tag{13c}$$

$$\frac{1}{2}\sin(2\theta)\frac{d\Phi}{dt} = k_R k\sin(2\theta) + \sqrt{2}\Omega_R\cos(2\theta)\cos\left(\frac{\Phi}{2}\right)\cos\left(\frac{\phi_\uparrow - \phi_\downarrow}{2}\right) - \frac{1}{3}g_s\eta\sin(2\theta)\cos(2\theta)[1 + \pi f(\eta)\cos(\Theta)], \tag{13d}$$

$$\frac{1}{2}\sin(2\theta)\frac{d\theta}{dt} = \frac{\sqrt{2}}{4}\Omega_R\sin(2\theta)\sin(\phi_\sigma - \phi_0) + \frac{1}{12}\pi g_s\eta f(\eta)\sin^2(2\theta)\sin(\Theta). \tag{13e}$$

For $k_R = 0$, Eqs. (13a) and (13c) describe nothing but the trap-driven center-of-mass oscillation of the solitary wave [32,33], and Eqs. (13d) and (13e) describe the well-known population oscillation of the solitary wave induced by the Raman coupling and the spin-dependent interaction. For $k_R \neq 0$, the STMC couples the population oscillation with the center-of-mass motion of the solitary wave.

From Eqs. (13d) and (13e), one can observe that if $\sin(2\theta) = 0$ and $\phi_\uparrow - \phi_\downarrow = n\pi$ with an integer n, the solutions of Eq. (13) are nothing but the two special uniaxial nematic solitary waves as we mentioned previously. On the other hand, for $\sin(2\theta) \neq 0$, all the wave functions are nonzero, and Eq. (13e) is self-consistent only when $\phi_\uparrow = \phi_\downarrow$. In this case, the spin vector is polarized in the x direction as

$$S_x = \sin(2\theta)\cos(\varphi),\ S_y = S_z = 0, \tag{14}$$

where $\varphi = \phi_{\uparrow,\downarrow} - \phi_0$, and the nematic matrix $\mathcal{N}$ is

$$\mathcal{N} = \begin{pmatrix}\frac{1}{3} & 0 & 0\\ 0 & \frac{1}{2}\cos(2\theta) - \frac{1}{6} & -\frac{1}{2}\sin(2\theta)\sin(\varphi)\\ 0 & -\frac{1}{2}\sin(2\theta)\sin(\varphi) & -\frac{1}{2}\cos(2\theta) - \frac{1}{6}\end{pmatrix}. \tag{15}$$

The eigenvalues of $\mathcal{N}$ are $\lambda_1 = \frac{1}{2}\sqrt{1 - S_x^2} - \frac{1}{6}$, $\lambda_2 = -\frac{1}{2}\sqrt{1 - S_x^2} - \frac{1}{6}$, and $\lambda_3 = \frac{1}{3}$, which indicate that the solitary wave with $\sin(2\theta) \neq 0$ is the biaxial nematic state with nonzero spin if $\cos(\varphi) \neq 0$, and hence we name it the spin-nematic solitary wave. Furthermore, for the spin-nematic solitary wave, we can immediately obtain the relation $S_x^2 + (\mathcal{N}_{yy} - \mathcal{N}_{zz})^2 + (2\mathcal{N}_{yz})^2 = 1$, which motivates us to construct

the vector $\mathbf{Q} = (Q_x, Q_y, Q_z)$, where Q_x, Q_y, and Q_z are

$$Q_x = S_x, \tag{16a}$$
$$Q_y = \mathcal{N}_{yy} - \mathcal{N}_{zz} = \cos(2\theta), \tag{16b}$$
$$Q_z = 2\mathcal{N}_{yz} = -\sin(2\theta)\sin(\varphi). \tag{16c}$$

The vector $\mathbf{Q}$ comprises the spin vector S_x and the nematic tensor $\mathcal{N}_{\nu\nu'}$, and hence we name it the spin-nematic vector, which lies on a unit Bloch sphere [77].

IV. DYNAMICS OF SPIN-NEMATIC SOLITARY WAVES FOR $g_s = 0$ WITHOUT TRAP

To highlight the effects of the STMC, we first neglect the harmonic trap and consider the simple case with $g_s = 0$. In this case, Eq. (13) reduces to

$$\frac{dk}{dt} = 0, \tag{17a}$$
$$\eta = -g_n/2, \tag{17b}$$
$$\frac{dz_c}{dt} = k - k_R \sin^2(\theta), \tag{17c}$$
$$\frac{d\varphi}{dt} = k_R k + \sqrt{2}\Omega_R \cot(2\theta)\cos(\varphi), \tag{17d}$$
$$\frac{d\theta}{dt} = \frac{\Omega_R}{\sqrt{2}}\sin(\varphi). \tag{17e}$$

Equation (17a) indicates that the momentum is conserved due to the translational symmetry of the system with $g_s = 0$. To understand this point, we make an infinitesimal translation δz_c for the center of mass, and then the Lagrangian after the translation becomes $\mathcal{L}(z_c + \delta z_c) = -\delta z_c \frac{dk}{dt} + \mathcal{L}$, which shows clearly that the translation invariance of the Lagrangian requires $\frac{dk}{dt} = 0$ as confirmed by Eq. (17a). Equation (17b) shows that η decouples from the other parameters and is determined completely by the strength of the spin-independent interaction. Since η^{-1} accounts for the width of the solitary wave, g_n should be negative, which coincides with the initial assumption $g_n < 0$.

With Eq. (17), we can further derive the equation of motion for the spin-nematic vector as

$$\frac{d}{dt}\begin{pmatrix} Q_x \\ Q_y \\ Q_z \end{pmatrix} = \begin{pmatrix} 0 & 0 & k_R k \\ 0 & 0 & \sqrt{2}\Omega_R \\ -k_R k & -\sqrt{2}\Omega_R & 0 \end{pmatrix}\begin{pmatrix} Q_x \\ Q_y \\ Q_z \end{pmatrix}, \tag{18}$$

which indicates that the Raman coupling and the STMC couple the spin vector with the nematic tensors linearly in the dynamical evolution. Equation (18) can also be written as $\frac{d\mathbf{Q}}{dt} = \mathbf{Q} \times \mathbf{B}_{\text{eff}}$, with $\mathbf{B}_{\text{eff}} = (\sqrt{2}\Omega_R, -k_R k, 0)$, which can be viewed as the extension of the Bloch equation for describing the precession of the spin-nematic vector on a unit Bloch sphere under the action of the effective field $\mathbf{B}_{\text{eff}}$.

A. Properties of ground-state solitary waves

We first study the ground-state solitary wave, in which the variational parameters are time independent and minimize the total energy. From the energy (12), both of the two special uniaxial nematic solitary waves with $\sin(2\theta) = 0$ should have energy higher than that of the spin-nematic solitary wave with $\sin(2\theta) \neq 0$ for the same momentum k, because the Raman coupling favors a nonzero spin to reduce the energy. Therefore, to obtain the ground-state solitary wave, we minimize the energy (12) with respect to the variational parameters under the constrained conditions $\sin(2\theta) \neq 0$ and $\phi_\uparrow = \phi_\downarrow$, which leads to the following algebraic equations for $g_s = 0$:

$$\theta = \pm \arcsin(\sqrt{k/k_R}), \tag{19a}$$
$$0 = k_R^2 k^4 - k_R^3 k^3 + 2\Omega_R^2 k^2 - 2\Omega_R^2 k_R k + \frac{1}{2}k_R^2\Omega_R^2, \tag{19b}$$
$$\varphi = n\pi, \tag{19c}$$
$$z_c = \text{arbitrary real number}, \tag{19d}$$

where n in Eq. (19c) is an integer. Actually, the ground-state solutions are nothing but the fixed points of Eq. (17). Equations (19a) and (19b) indicate that the amplitude of the ground-state solitary wave is related to its momentum, which depends on the strengths of the Raman coupling and the STMC. Equation (19d) demonstrates again that the ground-state solitary wave has translational symmetry for $g_s = 0$.

For simplicity, we consider $n = 0$, $z_c = 0$, and $0 < \theta < \pi/2$ for $\Omega_R \geqslant 0$ in the ground state. Figure 2 shows the ground-state properties of the solitary wave. We can observe that the ground-state solitary wave carries a finite momentum decreasing monotonically with Ω_R/k_R^2. The spin-nematic vector $Q_{x,y,z}$ indicates that the solitary wave has nonzero spin and nematicity simultaneously, and they are not independent of one another. The ground-state wave functions indicate that the parity of the real part of ψ_σ is opposite to that of the imaginary part, because the GP equations with $g_s = 0$ have joint symmetry $\hat{O} = \hat{P}\hat{K}$, where $\hat{P}$ and $\hat{K}$ are the parity and complex conjugate operators, respectively. We have also used the backward-forward Euler time discretization scheme to solve the imaginary-time propagation of the

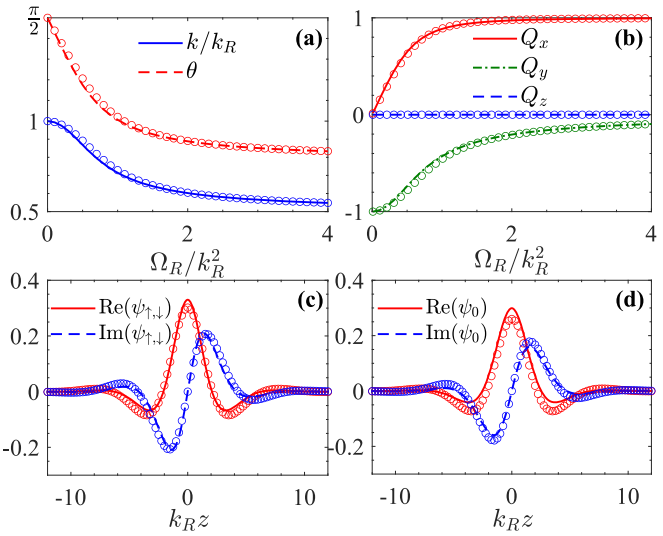

FIG. 2. (a) and (b) The parameters θ, k, and $Q_{x,y,z}$ in the ground state for different Ω_R/k_R^2 by fixing $g_n/k_R = -1$. (c) and (d) Real and imaginary parts of the ground-state wave functions at $\Omega_R/k_R^2 = 1$. The lines (solid line, dashed line, dash-dotted line) and the circles represent the results obtained by the GP simulations and variational calculations, respectively.

GP equation (6) numerically for obtaining the ground-state solitary wave solutions [80], where the time and space steps are $dt = 0.001$ and $dz = 0.1$, and the spatial derivative terms are computed by using the Fourier pseudo-spectral method, which is spectrally accurate. In the numerical computation, the iteration stops until $\mathrm{Max}[|\Psi_{n+1}(z) - \Psi_n(z)|] < 10^{-10}$ and $|E_{n+1} - E_n| < 10^{-10}$, where n represents the iterative number, and E is the total energy. The value of θ can be obtained in the GP simulations by defining $\int_{-\infty}^{+\infty} |\psi_0|^2 dz = \cos^2(\theta)$ and $\int_{-\infty}^{+\infty} |\psi_{\uparrow,\downarrow}|^2 dz = \frac{1}{2}\sin^2(\theta)$ due to the normalization condition of the wave functions, and the value of k is given by the average momentum. The results of the GP simulations are shown in Fig. 2, which agree well with the variational analysis.

Next, we perform the linear stability analysis of the ground-state solitary wave against a small perturbation based on Eq. (17). For this purpose, we set the variational parameter as $\zeta(t) = \zeta_g + \delta\zeta(t)$, where ζ_g represents the ground-state solution of the variational parameter, and $\delta\zeta(t)$ denotes the time-dependent deviation of the variational parameter from the ground-state solution. Substituting it into Eq. (17) and linearizing Eq. (17) around ζ_g, we obtain the ordinary differential equations

$$\frac{d}{dt}\begin{pmatrix}\delta k\\ \delta z_c\\ \delta\varphi\\ \delta\theta\end{pmatrix} = \begin{pmatrix}0 & 0 & 0 & 0\\ 1 & 0 & 0 & -k_R\sin(2\theta_g)\\ k_R & 0 & 0 & -\frac{2\sqrt{2}\Omega_R}{\sin^2(2\theta_g)}\\ 0 & 0 & \frac{\Omega_R}{\sqrt{2}} & 0\end{pmatrix}\begin{pmatrix}\delta k\\ \delta z_c\\ \delta\varphi\\ \delta\theta\end{pmatrix}. \quad (20)$$

Setting $\delta\zeta = |\zeta|e^{i\omega t}$ with the eigenfrequency ω and solving Eq. (20) yield the eigenmodes of the system with eigenvectors

$$\mathcal{V}_\pm = \begin{pmatrix}0\\ \pm i\frac{\sqrt{2}k_R\Omega_R}{\omega_\pm^2}\\ i\frac{\sqrt{2}}{\Omega_R}\omega_\pm\\ 1\end{pmatrix}, \quad \mathcal{V}_0 = \begin{pmatrix}0\\1\\0\\0\end{pmatrix}, \quad (21)$$

and eigenfrequencies

$$\omega_\pm = \pm\frac{\sqrt{2}\Omega_R}{\sin(2\theta_g)}, \quad \omega_0 = 0. \quad (22)$$

Since all the eigenfrequencies are real, $\delta\zeta$ will not grow or decay exponentially with time. The zero-energy mode with the frequency ω_0 and the eigenvector $\mathcal{V}_0$ is the Goldstone mode, which arises from the translational symmetry breaking of the solitary wave, and hence the solitary waves will move with no energy cost under perturbation. For the frequency $\omega_\pm$ corresponding to the eigenvector $\mathcal{V}_\pm$, the solitary waves will oscillate without damping, where the frequency $\omega_\pm$ depends on the strengths of the Raman coupling and the STMC as shown in Fig. 3(a).

We also solve the BdG equation (8) numerically to obtain the full low-energy excitation frequency. The results are shown in Fig. 3(b), which confirms that the ground-state solitary waves are dynamically stable under perturbation and will not grow or decay exponentially with time, since all the excitation frequencies are real. Since the BdG function has more degrees of freedom than the variational function, the BdG spectrum in Fig. 3(b) has many more modes than the variational result (22) [79]. For example, besides the Goldstone modes, there are two other zero-energy modes due to the global phase invariance.

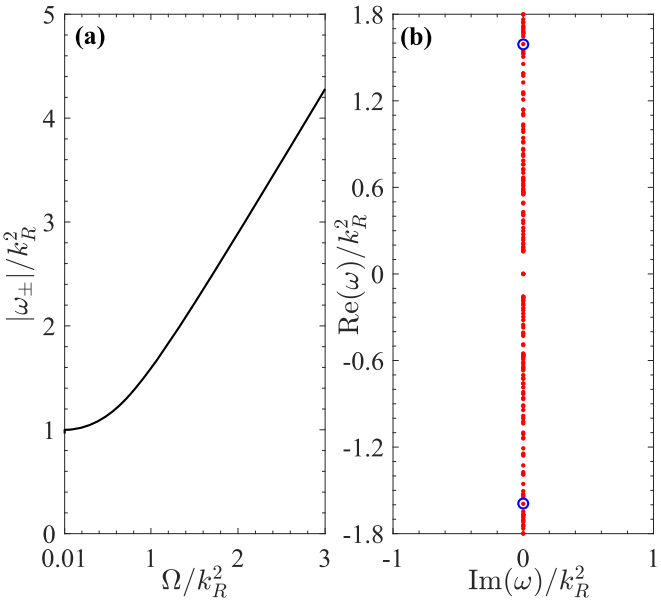

FIG. 3. (a) Frequency $\omega_\pm$ obtained by the variational approach as a function of Ω_R/k_R^2. (b) Bogoliubov excitation frequency ω for $\Omega_R/k_R^2 = 1$ and $g_n/k_R = -1$, where the two blue circles represent the frequency $\omega_\pm$ in Eq. (22) and the red points are obtained by the BdG equation.

B. Time evolutions of spin-nematic solitary waves

We explore the dynamical evolution of the spin-nematic solitary wave for $g_s = 0$ without a harmonic trap. Since the momentum is time independent, Eqs. (17) and (18) have exact solutions:

$$Q_x(t) = \frac{k_R k}{\sqrt{2}\Omega_R}\left[c_2\sin(\varpi t) - c_1\cos(\varpi t) + \frac{2\Omega_R^2}{k_R^2 k^2}c_0\right], \quad (23a)$$

$$Q_y(t) = c_2\sin(\varpi t) - c_1\cos(\varpi t) - c_0, \quad (23b)$$

$$Q_z(t) = \frac{\varpi}{\sqrt{2}\Omega_R}[c_1\sin(\varpi t) + c_2\cos(\varpi t)], \quad (23c)$$

$$z_c(t) = \frac{c_2 k_R}{\varpi}\sin^2\left(\frac{\varpi}{2}t\right) - \frac{c_1 k_R}{2\varpi}\sin(\varpi t) + v_0 t, \quad (23d)$$

with the time-independent constants

$$c_0 = \frac{k_R k}{\varpi^2}[\sqrt{2}\Omega_R\sin(2\theta_0)\cos(\varphi_0) - k_R k\cos(2\theta_0)], \quad (24a)$$

$$c_1 = -\frac{\Omega_R}{\varpi^2}[2\Omega_R\cos(2\theta_0) + \sqrt{2}k_R k\sin(2\theta_0)\cos(\varphi_0)], \quad (24b)$$

$$c_2 = -\frac{\sqrt{2}\Omega_R}{\varpi}\sin(2\theta_0)\sin(\varphi_0), \quad (24c)$$

$$v_0 = k - k_R(c_0 + 1)/2, \quad (24d)$$

$$\varpi = \sqrt{2\Omega_R^2 + k_R^2 k^2}, \quad (24e)$$

where θ_0 and φ_0 represent the initial values of θ and φ at $t = 0$, respectively. The solutions for the amplitude and the relative

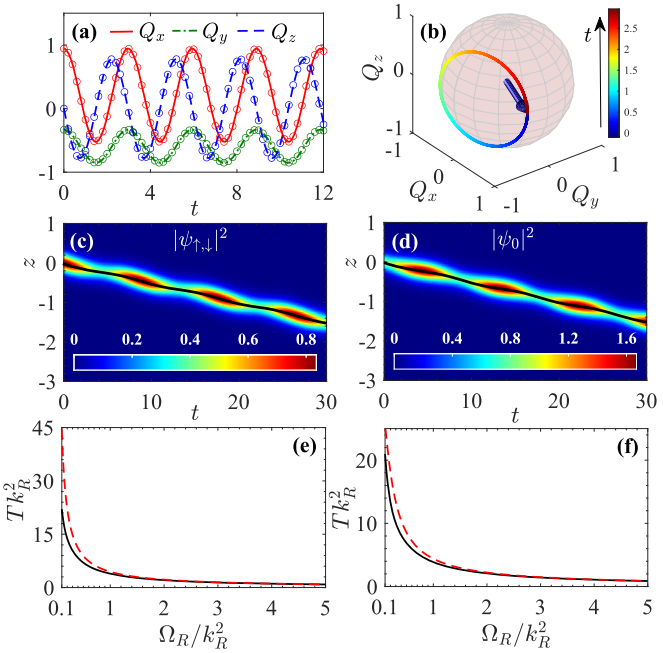

FIG. 4. Time evolution of the initially population-balanced solitary wave with $\theta_0 = \arccos(\sqrt{3}/3)$ and $\varphi_0 = 0$. (a) and (b) Time evolution of the spin-nematic vector for momentum $k = 4\Omega_R/k_R$. In panel (a), the solid red line, the dashed blue line, and the dash-dotted green line represent the numerical results of the GP simulations, and the circles are the results of the variational analysis. In panel (b), the blue arrow represents the spin-nematic vector at $t = 0$, the colored line is the trajectory of the spin-nematic vector, and the colorbar is the corresponding time. (c) and (d) Time evolution of the density for the initial momentum $k = 0$ obtained by the GP simulations. The solid black lines are the evolutions of the center of mass given by the variational analysis. The other parameters are $\Omega_R = 0.5$, $g_n = -10$, and $k_R = 0.1$ in panels (a)–(d). (e) and (f) Oscillation period T of the center of mass as a function of Ω_R/k_R^2 for $g_n/k_R = -10$. The momentum in panels (e) and (f) are $k/k_R = 0$ and $k/k_R = 0.2$, respectively. The solid black lines and the dashed red lines in panels (e) and (f) represent the periods given by the GP simulations and the variational analysis, respectively.

phase are $\theta(t) = \frac{1}{2}\arccos(Q_y)$ and $\varphi(t) = \arctan(-Q_z/Q_x)$, respectively.

Figure 4 shows the typical dynamical evolutions of the initially population-balanced solitary waves with $\theta_0 = \arccos(\sqrt{3}/3)$ and $\varphi_0 = 0$ for different initial momenta k. From Eqs. (23a)–(23c), if c_1 and c_2 are nonzero, as shown in Figs. 4(a) and 4(b), $Q_{x,y,z}$ oscillate periodically with the frequency ϖ, leading to the periodic flip of the spin-nematic vector along a closed circular orbit on the unit Bloch sphere. Equation (23d) indicates that the center-of-mass motion of the solitary wave can be viewed as the superposition of the linear motion with the constant velocity v_0 and the periodic motion with the frequency ϖ, as shown in Figs. 4(c) and 4(d). By using the second-order time-splitting Fourier pseudospectral method [81], we have also solved the GP equation (6) numerically by taking Eq. (9) as the initial wave functions. The GP simulations confirm the variational results as shown in Figs. 4(a)–(d).

To extract the intrinsic physical mechanism for the motion of the solitary wave, we rewrite the equation of motion for the center-of-mass coordinate in terms of the spin-nematic vector as

$$\frac{dz_c}{dt} = k - \frac{k_R}{2} + \frac{k_R}{2}Q_y. \tag{25}$$

The first two terms on the right-hand side of Eq. (25) indicate that the solitary wave would move with a constant velocity related to the STMC and the momentum. The last term accounts for the coupling between the center-of-mass momentum and the spin-nematic vector. With Eq. (18), we obtain the following relation:

$$\frac{d^2z_c}{dt^2} = \frac{k_R\Omega_R}{\sqrt{2}}Q_z. \tag{26}$$

This shows clearly that the solitary wave may experience a periodical force with strength $\propto \frac{k_R\Omega_R}{\sqrt{2}}Q_z$ for nonzero c_1 and c_2, which originates from the oscillation of Q_z. Thus, the interplay of the STMC and the Raman coupling induces the periodic flip of the spin-nematic vector under the action of an effective field $\mathbf{B}_{\text{eff}}$, and the periodic flip of the spin-nematic vector couples to the orbital motion of the solitary wave, manifesting the STMC effects clearly in the dynamics of solitary waves.

We have also performed the GP simulations for other system parameters and confirmed that the variational results can capture the essential physics effectively and provide the qualitative explanations for the dynamical evolutions of solitary waves under the action of the STMC and the Raman coupling. However, as shown in Figs. 4(e) and 4(f), for small Ω_R/k_R^2, the oscillation period T of the center of mass has quantitative difference between the numerical results and the variational results. We note that when Ω_R/k_R^2 is very small, as shown in Fig. 1(b), the single-particle energy band E_0 is close to the left and right sides of E_+ and E_-, respectively, and the atomic interactions may mix these different bands, leading to an additional oscillation in different energy bands [60]. Therefore, for small Ω_R/k_R^2, the variational wave functions need to be further optimized to capture the mixing effect, for example, considering the coherent superposition of the solitary waves in three energy bands [60].

V. DYNAMICS OF SPIN-NEMATIC SOLITARY WAVES FOR $g_s \neq 0$ WITHOUT A TRAP

When $g_s \neq 0$, Eqs. (12) and (13) are complicated, and it is difficult to obtain the analytical solutions. To analyze the effects of the spin-dependent interaction on the dynamics of solitary waves for $\gamma = 0$, we minimize the energy (12) numerically to obtain the ground-state solitary waves, and we use the fourth-order Runge-Kutta method to solve Eq. (13) numerically to study the dynamics of solitary waves.

Figure 5 shows the properties of the ground-state solitary waves for $g_s > 0$ and $g_s < 0$. We can observe that the variational parameters θ and k show features similar to those in the case of $g_s = 0$. Compared with the ground state for $g_s = 0$, the main difference is that, due to the relative phase $\varphi = 2n\pi$ for minimizing the Raman coupling energy, the center of mass must be a definite value, which indicates that the ground-state solitary wave does not have the translational symmetry

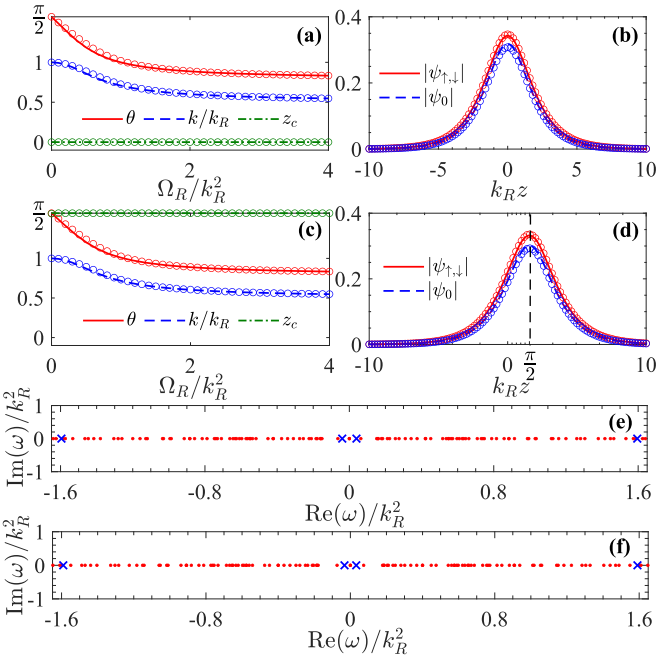

FIG. 5. Properties of the ground-state solitary waves for $g_s/k_R = -0.1$ [panels (a) and (b)] and $g_s/k_R = 0.1$ [panels (c) and (d)], where the strength of the spin-independent interaction is $g_n/k_R = -1$. Panels (a) and (c) show θ, k, and z_c for different Ω_R/k_R^2. Panels (b) and (d) show the norms of the ground-state wave functions for $\Omega_R/k_R^2 = 1$. In panels (a)–(d), the lines (solid line, dashed line, dash-dotted line) and circles represent the results obtained by the GP simulations and the variational calculations, respectively. Panels (e) and (f) show the Bogoliubov excitation frequencies (red points) given by the BdG equations for $g_s = -0.1$ and $g_s = 0.1$, respectively, where $\Omega_R/k_R^2 = 1$. The blue crosses represent the four excitation frequencies $\omega_{1,\pm}$ and $\omega_{2,\pm}$ given by the variational analysis.

due to the spatial-dependent exponential factors in the spin-dependent interaction terms. For example, if $\varphi = 0$ with $n = 0$, as shown in Fig. 5, the center of mass of the ground-state solitary wave should be $z_c = 0$ for $g_s < 0$ and $k_Rz_c = \frac{1}{2}\pi$ for $g_s > 0$, which can minimize the spin-dependent interaction energy. These results have also been confirmed by the imaginary-time evolution of the GP equation.

We further study the stabilities and the low-energy excitations of the ground-state solitary waves under the perturbation. In the presence of the spin-dependent interaction, after linearizing Eq. (13) around the ground-state solutions of the variational parameters, we have

$$\frac{d\delta\zeta}{dt} = \begin{pmatrix} 0 & g_s\varepsilon_2 & -\frac{g_s}{k_R}\varepsilon_2 & 0 \\ 1 & 0 & 0 & -k_R\sin(2\theta_g) \\ k_R & 0 & 0 & g_s\varepsilon_3 - \frac{2\sqrt{2}\Omega_R}{\sin^2(2\theta_g)} \\ 0 & g_s\varepsilon_1 & \frac{\sqrt{2}}{2}\Omega_R - g_s\frac{\varepsilon_1}{k_R} & 0 \end{pmatrix}\delta\zeta, \tag{27}$$

with the parameters

$$\epsilon_1 = \tfrac{1}{3}\pi k_R\eta f(\eta)\cos(2k_Rz_{c,g})\sin(2\theta_g), \tag{28a}$$

$$\epsilon_2 = \tfrac{1}{3}\pi k_R^2\eta f(\eta)\cos(2k_Rz_{c,g})\sin^2(2\theta_g), \tag{28b}$$

$$\epsilon_3 = \tfrac{2}{3}\eta[1 + \pi f(\eta)\cos(2k_Rz_{c,g})]\sin(2\theta_g), \tag{28c}$$

where $\delta\zeta = (\delta k, \delta z_c, \delta\varphi, \delta\theta)^T$ represents the deviations of the variational parameters from the ground-state solutions, and we have neglected the deviation of the width for a very weak spin-dependent interaction. The excitation frequency ω can be obtained by diagonalizing the 4×4 matrix on the right-hand side of Eq. (27), which has four nonzero pure real values denoted as $\omega_{1,\pm}$ and $\omega_{2,\pm}$ shown in Figs. 5(e) and 5(f). Therefore, if the solitary waves deviate from the ground states, they will oscillate stably without damping, and the motions of solitary waves would be the superposition between two different oscillations, where the frequencies $\omega_{1,\pm}$ and $\omega_{2,\pm}$ also depend on g_s. We have also solved the BdG equation (8) numerically. The typical low-energy excitation frequencies for $g_s < 0$ and $g_s > 0$ are shown in Figs. 5(e) and 5(f), respectively, which demonstrate that the ground-state solitary waves are dynamically stable. Moreover, the BdG spectrum also contains the zero-energy mode due to the global phase invariance.

Finally, we solve Eq. (13) numerically using the fourth-order Runge-Kutta method to study the motions of solitary waves in the presence of a weak spin-dependent interaction. Figure 6 shows the typical dynamical evolutions of the initially population-balanced solitary waves with $\theta_0 = \arccos(\sqrt{3}/3)$, $\varphi_0 = 0$, and $k_0 = 1$ for $g_s < 0$. From Eq. (13a), due to the lack of the translational symmetry, the momentum of the solitary wave is not conserved but changes with time as shown in Fig. 6(a). In particular, the spin-dependent interaction couples $Q_{x,y,z}$ nonlinearly in the dynamical evolution:

$$\frac{dQ_x}{dt} = \tfrac{1}{3}\pi g_s\eta f(\eta)Q_y[Q_x\sin(2k_Rz_c) + Q_z\cos(2k_Rz_c)] + k_Rk Q_z - \tfrac{1}{3}g_s\eta Q_yQ_z, \tag{29a}$$

$$\frac{dQ_y}{dt} = \sqrt{2}\Omega_RQ_z - \tfrac{1}{3}\pi g_s\eta f(\eta)\left(Q_x^2 - Q_z^2\right)\sin(2k_Rz_c) - \tfrac{2}{3}\pi g_s\eta f(\eta)Q_zQ_x\cos(2k_Rz_c), \tag{29b}$$

$$\frac{dQ_z}{dt} = \tfrac{1}{3}\pi g_s\eta f(\eta)Q_y[Q_x\cos(2k_Rz_c) - Q_z\sin(2k_Rz_c)] - k_Rk Q_x - \sqrt{2}\Omega_RQ_y + \tfrac{1}{3}g_s\eta Q_yQ_x. \tag{29c}$$

As shown in Figs. 6(b)–(d), the nonlinear coupling leads to the different oscillation frequencies of $Q_{x,y,z}$, and thus the trajectory of the spin-nematic vector on a unit Bloch sphere is not a closed orbit as shown in Fig. 6(e). Consequently, as shown by Eq. (25), besides the flip of the spin-nematic vector, the change of momentum also affects the center-of-mass motion of the solitary wave shown in Figs. 6(f)–(h). By using Eq. (9) as the initial wave functions, we have also solved the GP equation (6) numerically. Similar dynamical phenomena are also observed, and the variational results qualitatively agree with the results given by the GP simulations as shown in Fig. 6. However, the GP simulations show that the widths of solitary waves also change with time as shown in Figs. 6(f) and 6(g). It would be better to add a chirp term $\propto z^2$ to the phase of the variational wave function (9), which is generated intrinsically by the changes of the widths [79], and then the quantitative differences between the variational results and the numerical solutions of the GP equation may be further improved.

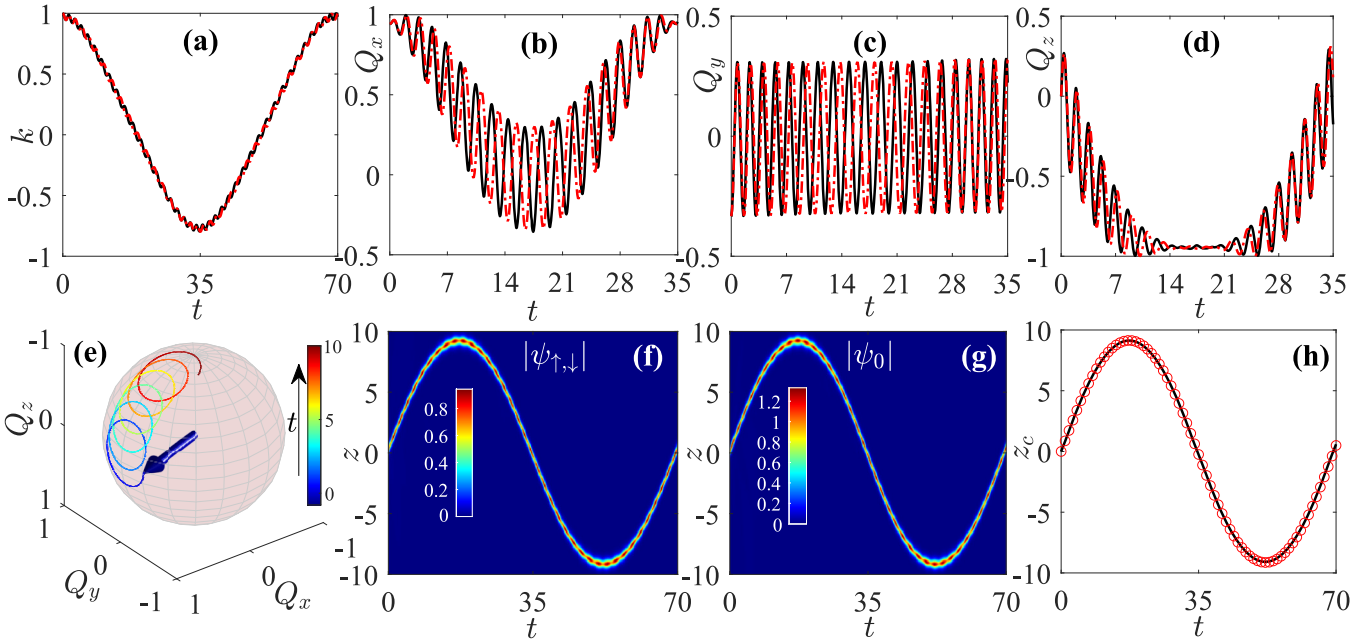

FIG. 6. Time evolution of the initially population-balanced solitary wave with $\theta_0 = \arccos(\sqrt{3}/3)$, $\varphi_0 = 0$, and $k_0 = 1$. (a) Momentum. (b)–(e) Spin-nematic vector. (f) and (g) Norms of the wave functions obtained by the GP simulations. (h) Center of mass. The parameters are $g_n = -10$, $g_s = -1$, $\Omega_R = 0.5$, and $k_R = 0.2$. In panel (e), the blue arrow represents the spin-nematic vector at $t = 0$, the colored line is the trajectory of the spin-nematic vector, and the colorbar is the corresponding time. In panels (a)–(d) and (h), the solid black lines represent the results given by the GP simulations, and the dash-dotted red lines and the red circles are the variational results.

VI. DYNAMICS OF SPIN-NEMATIC SOLITARY WAVES IN THE HARMONIC TRAP

In experiments, the BEC is usually confined in a harmonic trap, which also has a critical impact on the dynamics of solitary waves. Without the STMC, the ground-state solitary wave must localize at the center of the harmonic trap to minimize the trap energy, and the solitary wave oscillates with the trapping frequency in a harmonic trap [32,33]. It is, therefore, important to study the dynamics of the solitary waves under the combined action of the STMC and the harmonic trap.

We first study the ground-state solitary waves in the harmonic trap by setting all the variational parameters to be time independent and minimizing the energy (12) under the limitation $\sin(2\theta) \neq 0$. In the case of $g_s = 0$, the parameters k, θ, and φ in the ground state still satisfy Eqs. (19a)–(19c), but the center of mass of the ground-state solitary wave is located at the origin to minimize the trap energy, and the width η^{-1} satisfying the equation $4\eta^4 + 2g_n\eta^3 = \pi^2\gamma^2$ also depends on the trapping frequency γ. In the presence of the spin-dependent interaction, for $g_s < 0$, the variational parameters show features similar to those in the uniform case with $g_s < 0$ for a fixed γ. However, for $g_s > 0$, the trap will compete with the spin-dependent interaction in determining the center of mass of the ground-state solitary wave. As shown in Fig. 7(a), for $\Omega_R/k_R^2 \ll 1$, due to $\theta \sim \pi/2$, the spin-dependent interaction energy $\propto \sin^2(2\theta)$ is very small, and the solitary waves localize at the center of the trap. When Ω_R/k_R^2 surpasses a critical value, the spin-dependent interaction dominates and shifts the center of mass of the ground-state solitary wave to a nonzero value. Thus, for $g_s > 0$, in a harmonic trap, the center of mass of the ground-state solitary wave experiences a transition from zero to nonzero value with increasing Ω_R/k_R^2. As shown in Fig. 7(a), the variationally predicted critical point for Ω_R/k_R^2 deviates from the one given by the GP simulation, which can be improved by using a better function as the variational ansatz. Moreover, when Ω_R/k_R^2 surpasses the critical point, the stationary solitary wave with $z_c = 0$ can actually exist as shown in Fig. 7(b), but becomes unstable under a perturbation as shown in Figs. 7(c) and 7(d).

Finally, we study the motions of solitary waves under the combined action of the STMC and the harmonic trap. From Eqs. (13a), (13c), and (13e), we can get

$$\frac{d^2 z_c}{dt^2} = \frac{k_R \Omega_R}{\sqrt{2}} Q_z - \gamma^2 z_c, \tag{30}$$

which indicates that the solitary wave experiences a linear restoring force produced by the harmonic trap, in addition to the force given by the STMC. The general solution of Eq. (30) is

$$z_c(t) = \frac{c}{\gamma}\sin(\gamma t) + \frac{k_R \Omega_R}{\sqrt{2}\gamma}\int_0^t \sin[\gamma(t-t')]Q_z(t')dt', \tag{31}$$

where we have assumed $z_c(t=0) = 0$, $c = k_0 + k_R(Q_{y,0} - 1)/2$ is a time-independent constant, and k_0 and $Q_{y,0}$ represent the initial values of the momentum k and the spin-nematic vector Q_y, respectively. It is obvious that the harmonic trap will induce an additional center-of-mass oscillation with period $2\pi/\gamma$.

To further clarify the combined effects of the trap and the STMC on the motions of solitary waves, we use Eq. (9) as the initial wave functions to solve the GP equation (6) numerically. Figures 8(a)–(c) show the dynamical evolutions

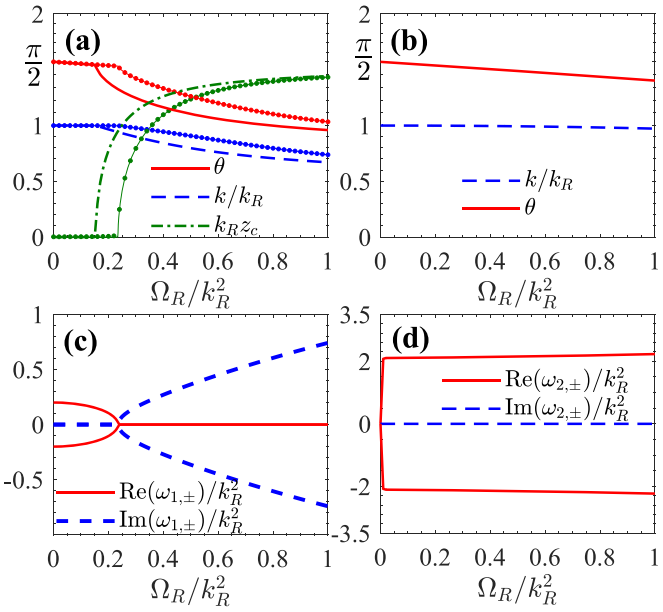

FIG. 7. (a) and (b) Parameters θ, k, and z_c in the harmonically trapped ground-state solitary wave for different Ω_R/k_R^2. The solid red line, the dashed blue line, and the dash-dotted green line are the results given by the GP simulations, and the red, blue, and green lines with solid circles are the results of the variational analysis. (b) Parameters θ and k in the stationary solitary wave with $z_c = 0$ for different Ω_R/k_R^2, which are obtained by solving the time-independent equation (13). (c) and (d) The excitation frequencies $\omega_{1,\pm}$ and $\omega_{2,\pm}$ of the stationary solitary wave with $z_c = 0$ for different Ω_R/k_R^2, which are obtained by the linear stability analysis of Eq. (13). In panels (a)–(d), the other system parameters are $g_n/k_R = -10$, $g_s/k_R = 1$, and $\gamma/k_R^2 = 0.2$.

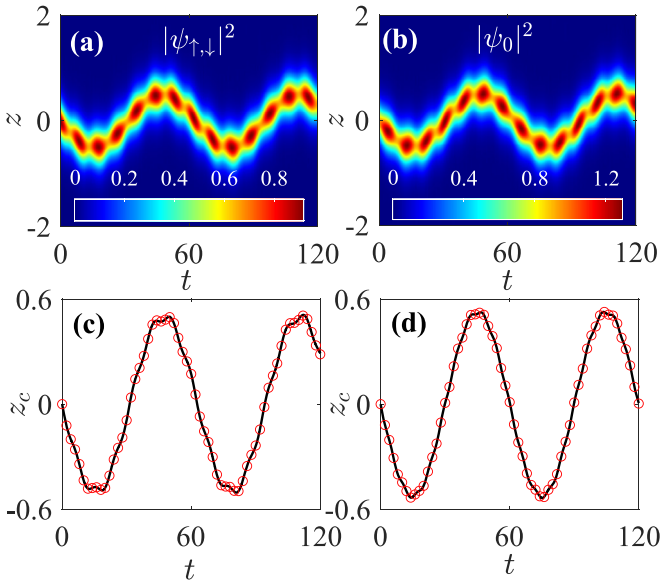

FIG. 8. Time evolution of the initially population-balanced solitary wave in the harmonic trap with $\gamma = 0.1$. (a)–(c) Time evolutions of the densities and the center of mass for $g_s = 0$, where the parameters are $g_n = -10$, $\Omega_R = 0.5$, and $k_R = 0.1$. (d) Evolution of the center of mass for $g_s = -0.1$. The other parameters are the same as those in panels (a)–(c). Panels (a) and (b) are given by the GP simulations, and the solid black lines and the red circles in panels (c) and (d) represent the results of the GP simulations and the variational analysis, respectively.

of the initially population-balanced solitary waves for $g_s = 0$. We can observe that the solitary waves display two different oscillations. To distinguish these two different oscillations, we take the solution (23c) as the approximation for Q_z in a weak harmonic trap with $\gamma \ll 1$, and the center of mass can be approximated as follows:

$$z_c \simeq \frac{c - \varpi\alpha_1}{\gamma}\sin(\gamma t) - \alpha_2\cos(\gamma t) + \alpha\sin(\varpi t + \beta), \tag{32}$$

where the constants are $\alpha = \sqrt{\alpha_1^2 + \alpha_2^2}$ and $\beta = \arctan(\alpha_2/\alpha_1)$, with $\alpha_{1,2} = c_{1,2}k_R\varpi/(2\gamma^2 - 2\varpi^2)$. Equation (32) shows clearly that the first two terms are the trap-driven oscillations with the frequency γ, and the last term is the STMC-driven oscillation with the frequency ϖ. Therefore, the motions of solitary waves can be viewed as the superposition of the trap-driven oscillation and the STMC-driven oscillation, as shown in Figs. 8(a)–(c). For $g_s \neq 0$, we have also performed the GP simulation for a weak harmonic trap and obtained a similar result, as shown in Fig. 8(d).

VII. CONCLUSIONS

In summary, we have investigated the dynamics of bright solitary waves in the spin-tensor-momentum coupled spin-1 BEC. By using the variational method and the numerical simulation of the GP equation, the properties of stationary and moving bright solitary waves were explored analytically and numerically. We found that the solitary waves have nonzero spin and nematicity simultaneously, and hence they are termed spin-nematic solitary waves. The ground-state solitary wave carries a finite momentum due to the STMC, and the low-energy excitations contain the zero-energy modes and oscillation modes with frequencies related to the STMC and the Raman coupling. The equations of motion for the variational parameters show that the spin-nematic vector couples with the center-of-mass coordinate, and the interplay of the STMC and the Raman coupling induces the flip of the spin-nematic vector on a unit Bloch sphere, which in turn provides a force to drive the solitary waves to oscillate, leading to the STMC effects in the motions of solitary waves. In the presence of a harmonic trap, it competes with the spin-dependent interaction in determining the center of mass of the solitary wave and induces an additional collective oscillation with frequency related to the trapping frequency. These analytical results were also confirmed by the direct numerical simulations of the GP equations. The present study may also be extended to the case of dark solitary waves for the repulsive spin-dependent atomic interaction. We believe that these interesting dynamical features of solitary waves affected by the STMC can be observed in future experiments.

ACKNOWLEDGMENTS

We sincerely acknowledge Qing Sun, Deng-Shan Wang, and Wei Han for helpful discussions. This work was supported by the National Natural Science Foundation of China (Grants No. 11875010, No. 12175027, No. 12175129, and No. 12171041); by the Natural Science Foundation of Chongqing (Grants No. cstc2019jcyj-msxmX0217 and No. cstc2021jcyj-msxmX0168); by the Key Research Program of Frontier Sciences of Chinese Academy of Sciences (Grant No. ZDBS-LY-7016); and by the Japan Society for the Promotion of Science, KAKENHI Grant No. 20K03804.

APPENDIX: THE PARAMETERS IN THE BdG EQUATION

In the BdG equation (8), the parameters are $A = A_1 + g_+A_2 + 2g_sA_3 - \frac{\Omega_R}{\sqrt{2}}F_x$ and $B = -g_+B_1 - B_2 - g_sB_3$, with $g_\pm = g_n \pm g_s$. The matrices A_j and B_j with $j = 1$, 2, and 3 are

$$A_1 = \begin{pmatrix} h_\uparrow & 0 & g_-\psi_{\uparrow,0}\psi^*_{\downarrow,0} \\ 0 & h_0 & 0 \\ g_-\psi^*_{\uparrow,0}\psi_{\downarrow,0} & 0 & h_\downarrow \end{pmatrix}, \tag{A1}$$

$$A_2 = \begin{pmatrix} 0 & \psi_{\uparrow,0}\psi^*_{0,0} & 0 \\ \psi^*_{\uparrow,0}\psi_{0,0} & 0 & \psi_{0,0}\psi^*_{\downarrow,0} \\ 0 & \psi^*_{0,0}\psi_{\downarrow,0} & 0 \end{pmatrix}, \tag{A2}$$

$$A_3 = \begin{pmatrix} 0 & \kappa\psi_{0,0}\psi^*_{\downarrow,0} & 0 \\ \kappa^*\psi^*_{0,0}\psi_{\downarrow,0} & 0 & \kappa^*\psi_{\uparrow,0}\psi^*_{0,0} \\ 0 & \kappa\psi^*_{\uparrow,0}\psi_{0,0} & 0 \end{pmatrix}, \tag{A3}$$

$$B_1 = \begin{pmatrix} \psi^2_{\uparrow,0} & \psi_{\uparrow,0}\psi_{0,0} & 0 \\ \psi_{\uparrow,0}\psi_{0,0} & 0 & \psi_{0,0}\psi_{\downarrow,0} \\ 0 & \psi_{0,0}\psi_{\downarrow,0} & \psi^2_{\downarrow,0} \end{pmatrix}, \tag{A4}$$

$$B_2 = \begin{pmatrix} 0 & 0 & g_-\psi_{\uparrow,0}\psi_{\downarrow,0} \\ 0 & g_n\psi^2_{0,0} & 0 \\ g_-\psi_{\uparrow,0}\psi_{\downarrow,0} & 0 & 0 \end{pmatrix}, \tag{A5}$$

$$B_3 = \begin{pmatrix} 0 & 0 & \kappa\psi^2_{0,0} \\ 0 & 2\kappa^*\psi_{\uparrow,0}\psi_{\downarrow,0} & 0 \\ \kappa\psi^2_{0,0} & 0 & 0 \end{pmatrix}, \tag{A6}$$

where $\kappa = e^{i2k_Rz}$, and the h_σ's with $\sigma = \uparrow$, 0, and $\downarrow$ are

$$h_\uparrow = h + ik_R\frac{\partial}{\partial z} + g_+(2\rho_{\uparrow,0} + \rho_{0,0}) + g_-\rho_{\downarrow,0} - \mu, \tag{A7}$$

$$h_0 = h + g_+\rho_{T,0} + g_-\rho_{0,0} - \mu, \tag{A8}$$

$$h_\downarrow = h + ik_R\frac{\partial}{\partial z} + g_+(\rho_{0,0} + 2\rho_{\downarrow,0}) + g_-\rho_{\uparrow,0} - \mu, \tag{A9}$$

with $h = -\frac{1}{2}\frac{\partial^2}{\partial z^2} + \frac{1}{2}\gamma^2z^2$ and $\rho_{T,0} = \sum_\sigma \rho_{\sigma,0}$, where $\rho_{\sigma,0} = |\psi_{\sigma,0}|^2$ is the total density of the ground state. The chemical potential μ is

$$\mu = \int_{-\infty}^{+\infty} \left[\Psi^\dagger\mathcal{H}\Psi + g_n\rho^2_{T,0} + g_s(\rho_{\uparrow,0} - \rho_{\downarrow,0})^2 + 2g_s\left|e^{ik_Rz}\psi^*_{\uparrow,0}\psi_{0,0} + e^{-ik_Rz}\psi^*_{0,0}\psi_{\downarrow,0}\right|^2\right]dz, \tag{A10}$$

where $\mathcal{H} = h + ik_RF_z\frac{\partial}{\partial z} - \frac{\Omega_R}{\sqrt{2}}F_x$; $\Psi = (\psi_{\uparrow,0}, \psi_{0,0}, \psi_{\downarrow,0})^T$, with T being the transpose; and the superscripts $*$ and $\dagger$ represent the conjugate and the conjugate transpose, respectively.

[1] J. Dalibard, F. Gerbier, G. Juzeliūnas, and P. Öhberg, Artificial gauge potentials for neutral atoms, Rev. Mod. Phys. **83**, 1523 (2011).

[2] Y. J. Lin, K. Jiménez-García, and I. B. Spielman, Spin-orbit-coupled Bose-Einstein condensates, Nature (London) **471**, 83 (2011).

[3] J. Y. Zhang, S. C. Ji, Z. Chen, L. Zhang, Z. D. Du, B. Yan, G. S. Pan, B. Zhao, Y. J. Deng, H. Zhai, S. Chen, and J. W. Pan, Collective Dipole Oscillations of a Spin-Orbit Coupled Bose-Einstein Condensate, Phys. Rev. Lett. **109**, 115301 (2012).

[4] P. Wang, Z. Q. Yu, Z. Fu, J. Miao, L. Huang, S. Chai, H. Zhai, and J. Zhang, Spin-Orbit Coupled Degenerate Fermi Gases, Phys. Rev. Lett. **109**, 095301 (2012).

[5] L. W. Cheuk, A. T. Sommer, Z. Hadzibabic, T. Yefsah, W. S. Bakr, and M. W. Zwierlein, Spin-Injection Spectroscopy of a Spin-Orbit Coupled Fermi Gas, Phys. Rev. Lett. **109**, 095302 (2012).

[6] L. Huang, Z. Meng, P. Wang, P. Peng, S.-L. Zhang, L. Chen, D. Li, Q. Zhou, and J. Zhang, Experimental realization of two-dimensional synthetic spin-orbit coupling in ultracold Fermi gases, Nat. Phys. **12**, 540 (2016).

[7] Z. Wu, L. Zhang, W. Sun, X.-T. Xu, B.-Z. Wang, S.-C. Ji, Y. Deng, S. Chen, X.-J. Liu, and J.-W. Pan, Realization of two-dimensional spin-orbit coupling for Bose-Einstein condensates, Science **354**, 83 (2016).

[8] V. Galitski and I. B. Spielman, Spin-orbit coupling in quantum gases, Nature (London) **494**, 49 (2013).

[9] H.-R. Chen, K.-Y. Lin, P.-K. Chen, N.-C. Chiu, J.-B. Wang, C.-A. Chen, P.-P. Huang, S.-K. Yip, Y. Kawaguchi, and Y.-J. Lin, Spin-Orbital-Angular-Momentum Coupled Bose-Einstein Condensates, Phys. Rev. Lett. **121**, 113204 (2018).

[10] P.-K. Chen, L.-R. Liu, M.-J. Tsai, N.-C. Chiu, Y. Kawaguchi, S.-K. Yip, M.-S. Chang, and Y.-J. Lin, Rotating Atomic Quantum Gases with Light-Induced Azimuthal Gauge Potentials and the Observation of the Hess-Fairbank Effect, Phys. Rev. Lett. **121**, 250401 (2018).

[11] D. Zhang, T. Gao, P. Zou, L. Kong, R. Li, X. Shen, X.-L. Chen, S.-G. Peng, M. Zhan, H. Pu, and K. Jiang, Ground-State Phase Diagram of a Spin-Orbital-Angular-Momentum Coupled Bose-Einstein Condensate, Phys. Rev. Lett. **122**, 110402 (2019).

[12] J.-R. Li, J. Lee, W. Huang, S. Burchesky, B. Shteynas, F. C. Top, A. O. Jamison, and W. Ketterle, A stripe phase with supersolid properties in spin-orbit-coupled Bose-Einstein condensates, Nature (London) **543**, 91 (2017).

[13] T.-L. Ho and S. Z. Zhang, Bose-Einstein Condensates with Spin-Orbit Interaction, Phys. Rev. Lett. **107**, 150403 (2011).

[14] Y. Li, L. P. Pitaevskii, and S. Stringari, Quantum Tricriticality and Phase Transitions in Spin-Orbit Coupled Bose-Einstein Condensates, Phys. Rev. Lett. **108**, 225301 (2012).

[15] C. J. Wang, C. Gao, C.-M. Jian, and H. Zhai, Spin-Orbit Coupled Spinor Bose-Einstein Condensates, Phys. Rev. Lett. **105**, 160403 (2010).

[16] X.-F. Zhang, L. Wen, L.-X. Wang, G.-P. Chen, R.-B. Tan, and H. Saito, Spin-orbit-coupled Bose gases with nonlocal Rydberg interactions held under a toroidal trap, Phys. Rev. A **105**, 033306 (2022).

[17] H. Hu, L. Jiang, X. J. Liu, and H. Pu, Probing Anisotropic Superfluidity in Atomic Fermi Gases with Rashba Spin-Orbit Coupling, Phys. Rev. Lett. **107**, 195304 (2011).

[18] C. Qu, Z. Zheng, M. Gong, Y. Xu, L. Mao, X. Zou, G. Guo, and C. Zhang, Topological superfluids with finite-momentum pairing and Majorana fermions, Nat. Commun. **4**, 2710 (2013).

[19] W. Zhang and W. Yi, Topological Fulde-Ferrell-Larkin-Ovchinnikov states in spin-orbit-coupled Fermi gases, Nat. Commun. **4**, 2711 (2013).

[20] J. P. A. Devreese, J. Tempere, and C. A. R. Sá de Melo, Effects of Spin-Orbit Coupling on the Berezinskii-Kosterlitz-Thouless Transition and the Vortex-Antivortex Structure in Two-Dimensional Fermi Gases, Phys. Rev. Lett. **113**, 165304 (2014).

[21] K. Sun, C. Qu, and C. Zhang, Spin-orbital-angular-momentum coupling in Bose-Einstein condensates, Phys. Rev. A **91**, 063627 (2015).

[22] C. Qu, K. Sun, and C. Zhang, Quantum phases of Bose-Einstein condensates with synthetic spin-orbital-angular-momentum coupling, Phys. Rev. A **91**, 053630 (2015).

[23] M. DeMarco and H. Pu, Angular spin-orbit coupling in cold atoms, Phys. Rev. A **91**, 033630 (2015).

[24] Q. Sun, L. Wen, W.-M. Liu, G. Juzeliūnas, and A.-C. Ji, Tunneling-assisted spin-orbit coupling in bilayer Bose-Einstein condensates, Phys. Rev. A **91**, 033619 (2015).

[25] S. Sinha, R. Nath, and L. Santos, Trapped Two-Dimensional Condensates with Synthetic Spin-Orbit Coupling, Phys. Rev. Lett. **107**, 270401 (2011).

[26] H. Hu, B. Ramachandhran, H. Pu, and X.-J. Liu, Spin-Orbit Coupled Weakly Interacting Bose-Einstein Condensates in Harmonic Traps, Phys. Rev. Lett. **108**, 010402 (2012).

[27] S. Burger, K. Bongs, S. Dettmer, W. Ertmer, K. Sengstock, A. Sanpera, G. V. Shlyapnikov, and M. Lewenstein, Dark Solitons in Bose-Einstein Condensates, Phys. Rev. Lett. **83**, 5198 (1999).

[28] K. E. Strecker, G. B. Partridge, A. G. Truscott, and R. G. Hulet, Formation and Propagation of Matter Wave Soliton Trains, Nature (London) **417**, 150 (2002).

[29] L. Khaykovich, F. Schreck, G. Ferrari, T. Bourdel, J. Cubizolles, L. D. Carr, Y. Castin, and C. Salomon, Formation of a matter-wave bright soliton, Science **296**, 1290 (2002).

[30] S. L. Cornish, S. T. Thompson, and C. E. Wieman, Formation of Bright Matter-Wave Solitons during the Collapse of Attractive Bose-Einstein Condensates, Phys. Rev. Lett. **96**, 170401 (2006).

[31] B. J. Dąbrowska-Wüster, E. A. Ostrovskaya, T. J. Alexander, and Y. S. Kivshar, Multicomponent gap solitons in spinor Bose-Einstein condensates, Phys. Rev. A **75**, 023617 (2007).

[32] C. Becker, S. Stellmer, P. Soltan-Panahi, S. Dörscher, M. Baumert, E.-M. Richter, J. Kronjäger, K. Bongs, and K. Sengstock, Oscillations and interactions of dark and dark-bright solitons in Bose-Einstein condensates, Nat. Phys. **4**, 496 (2008).

[33] A. Weller, J. P. Ronzheimer, C. Gross, J. Esteve, M. K. Oberthaler, D. J. Frantzeskakis, G. Theocharis, and P. G. Kevrekidis, Experimental Observation of Oscillating and Interacting Matter Wave Dark Solitons, Phys. Rev. Lett. **101**, 130401 (2008).

[34] C. Hamner, J. J. Chang, P. Engels, and M. A. Hoefer, Generation of Dark-Bright Soliton Trains in Superfluid-Superfluid Counterflow, Phys. Rev. Lett. **106**, 065302 (2011).

[35] C. Hamner, Y. Zhang, J. J. Chang, C. Zhang, and P. Engels, Phase Winding a Two-Component Bose-Einstein Condensate in an Elongated Trap: Experimental Observation of Moving Magnetic Orders and Dark-Bright Solitons, Phys. Rev. Lett. **111**, 264101 (2013).

[36] A. L. Marchant, T. P. Billam, T. P. Wiles, M. M. H. Yu, S. Gardiner, and S. L. Cornish, Controlled formation and reflection of a bright solitary matter wave, Nat. Commun. **4**, 1865 (2013).

[37] J. H. V. Nguyen, P. Dyke, D. Luo, B. A. Malomed, and R. G. Hulet, Collisions of matter-wave solitons, Nat. Phys. **10**, 918 (2014).

[38] A. R. Fritsch, M. Lu, G. H. Reid, A. M. Piñeiro, and I. B. Spielman, Creating solitons with controllable and near-zero velocity in Bose-Einstein condensates, Phys. Rev. A **101**, 053629 (2020).

[39] T. Yefsah, A. T. Sommer, M. J. H. Ku, L. W. Cheuk, W. Ji, W. S. Bakr, and M. W. Zwierlein, Heavy solitons in a fermionic superfluid, Nature (London) **499**, 426 (2013).

[40] M. J. H. Ku, W. Ji, B. Mukherjee, E. Guardado-Sanchez, L. W. Cheuk, T. Yefsah, and M. W. Zwierlein, Motion of a Solitonic Vortex in the BEC-BCS Crossover, Phys. Rev. Lett. **113**, 065301 (2014).

[41] N. J. Zabusky and M. D. Kruskal, Interaction of "Solitons" in a Collisionless Plasma and the Recurrence of Initial States, Phys. Rev. Lett. **15**, 240 (1965).

[42] Y. Xu, Y. Zhang, and B. Wu, Bright solitons in spin-orbit-coupled Bose-Einstein condensates, Phys. Rev. A **87**, 013614 (2013).

[43] V. Achilleos, D. J. Frantzeskakis, P. G. Kevrekidis, and D. E. Pelinovsky, Matter-Wave Bright Solitons in Spin-Orbit Coupled Bose-Einstein Condensates, Phys. Rev. Lett. **110**, 264101 (2013).

[44] Y. V. Kartashov, V. V. Konotop, and F. K. Abdullaev, Gap Solitons in a Spin-Orbit-Coupled Bose-Einstein Condensate, Phys. Rev. Lett. **111**, 060402 (2013).

[45] Y. V. Kartashov, V. V. Konotop, and D. A. Zezyulin, Bose-Einstein condensates with localized spin-orbit coupling: Soliton complexes and spinor dynamics, Phys. Rev. A **90**, 063621 (2014).

[46] Y. Zhang, Y. Xu, and T. Busch, Gap solitons in spin-orbit-coupled Bose-Einstein condensates in optical lattices, Phys. Rev. A **91**, 043629 (2015).

[47] S. Peotta, F. Mireles, and M. D. Ventra, Edge binding of sine-Gordon solitons in spin-orbit-coupled Bose-Einstein condensates, Phys. Rev. A **91**, 021601(R) (2015).

[48] H. Sakaguchi, B. Li, and B. A. Malomed, Creation of two-dimensional composite solitons in spin-orbit-coupled self-attractive Bose-Einstein condensates in free space, Phys. Rev. E **89**, 032920 (2014).

[49] L. Salasnich, W. B. Cardoso, and B. A. Malomed, Localized modes in quasi-two-dimensional Bose-Einstein condensates with spin-orbit and Rabi couplings, Phys. Rev. A **90**, 033629 (2014).

[50] V. E. Lobanov, Y. V. Kartashov, and V. V. Konotop, Fundamental, Multipole, and Half-Vortex Gap Solitons in Spin-Orbit Coupled Bose-Einstein Condensates, Phys. Rev. Lett. **112**, 180403 (2014).

[51] L. Wen, Q. Sun, Y. Chen, D.-S. Wang, J. Hu, H. Chen, W. M. Liu, G. Juzeliūnas, B. A. Malomed, and A.-C. Ji, Motion of solitons in one-dimensional spin-orbit-coupled Bose-Einstein condensates, Phys. Rev. A **94**, 061602(R) (2016).

[52] Y. C. Zhang, Z. W. Zhou, B. A. Malomed, and H. Pu, Stable Solitons in Three Dimensional Free Space without the Ground State: Self-Trapped Bose-Einstein Condensates with Spin-Orbit Coupling, Phys. Rev. Lett. **115**, 253902 (2015).

[53] Y. V. Kartashov and V. V. Konotop, Solitons in Bose-Einstein Condensates with Helicoidal Spin-Orbit Coupling, Phys. Rev. Lett. **118**, 190401 (2017).

[54] S. Gautam and S. K. Adhikari, Vortex-bright solitons in a spin-orbit-coupled spin-1 condensate, Phys. Rev. A **95**, 013608 (2017).

[55] S. Gautam and S. K. Adhikari, Three-dimensional vortex-bright solitons in a spin-orbit-coupled spin-1 condensate, Phys. Rev. A **97**, 013629 (2018).

[56] S. K. Adhikari, Phase separation of vector solitons in spin-orbit-coupled spin-1 condensates, Phys. Rev. A **100**, 063618 (2019).

[57] S. Gautam and S. K. Adhikari, Vector solitons in a spin-orbit coupled spin-2 Bose-Einstein condensate, Phys. Rev. A **91**, 063617 (2015).

[58] Sh. Mardonov, V. V. Konotop, B. A. Malomed, M. Modugno, and E. Ya. Sherman, Spin-orbit-coupled soliton in a random potential, Phys. Rev. A **98**, 023604 (2018).

[59] Y. V. Kartashov and D. A. Zezyulin, Stable Multiring and Rotating Solitons in Two-Dimensional Spin-Orbit-Coupled Bose-Einstein Condensates with a Radially Periodic Potential, Phys. Rev. Lett. **122**, 123201 (2019).

[60] V. Achilleos, D. J. Frantzeskakis, and P. G. Kevrekidis, Beating dark-dark solitons and *Zitterbewegung* in spin-orbit-coupled Bose-Einstein condensates, Phys. Rev. A **89**, 033636 (2014).

[61] H. Sakaguchi and B. A. Malomed, Flipping-shuttle oscillations of bright one- and two-dimensional solitons in spin-orbit-coupled Bose-Einstein condensates with Rabi mixing, Phys. Rev. A **96**, 043620 (2017).

[62] E. Chiquillo, Quasi-one-dimensional spin-orbit- and Rabi-coupled bright dipolar Bose-Einstein-condensate solitons, Phys. Rev. A **97**, 013614 (2018).

[63] O. Fialko, J. Brand, and U. Zülicke, Soliton magnetization dynamics in spin-orbit-coupled Bose-Einstein condensates, Phys. Rev. A **85**, 051605(R) (2012).

[64] F. Kh. Abdullaev, M. Brtka, A. Gammal, and L. Tomio, Solitons and Josephson-type oscillations in Bose-Einstein condensates with spin-orbit coupling and time-varying Raman frequency, Phys. Rev. A **97**, 053611 (2018).

[65] T. Mithun, A. R. Fritsch, G. N. Koutsokostas, D. J. Frantzeskakis, I. B. Spielman, and P. G. Kevrekidis, Stationary solitons in F = 1 spin-orbit coupled Bose-Einstein condensates, arXiv:2212.12966.

[66] Y. Xu, L. Mao, B. Wu, and C. Zhang, Dark Solitons with Majorana Fermions in Spin-Orbit-Coupled Fermi Gases, Phys. Rev. Lett. **113**, 130404 (2014).

[67] P. Zou, J. Brand, X.-J. Liu, and H. Hu, Traveling Majorana Solitons in a Low-Dimensional Spin-Orbit-Coupled Fermi Superfluid, Phys. Rev. Lett. **117**, 225302 (2016).

[68] X.-J. Liu, Soliton-induced Majorana fermions in a one-dimensional atomic topological superfluid, Phys. Rev. A **91**, 023610 (2015).

[69] A. Muñoz Mateo and X. Yu, Two types of dark solitons in a spin-orbit-coupled Fermi gas, Phys. Rev. A **105**, L021301 (2022).

[70] D. Li, L. Huang, P. Peng, G. Bian, P. Wang, Z. Meng, L. Chen, and J. Zhang, Experimental realization of spin-tensor momentum coupling in ultracold Fermi gases, Phys. Rev. A **102**, 013309 (2020).

[71] X.-W. Luo, K. Sun, and C. Zhang, Spin-Tensor–Momentum-Coupled Bose-Einstein Condensates, Phys. Rev. Lett. **119**, 193001 (2017).

[72] H. Hu, J. Hou, F. Zhang, and C. Zhang, Topological Triply Degenerate Points Induced by Spin-Tensor-Momentum Couplings, Phys. Rev. Lett. **120**, 240401 (2018).

[73] J. Sun, Y. Chen, X. Chen, and Y. Zhang, Bright solitons in a spin-tensor-momentum-coupled Bose-Einstein condensate, Phys. Rev. A **101**, 053621 (2020).

[74] R. B. Diener and T.-L. Ho, ^{52}Cr Spinor Condensate: A Biaxial or Uniaxial Spin Nematic, Phys. Rev. Lett. **96**, 190405 (2006).

[75] E. J. Mueller, Spin textures in slowly rotating Bose-Einstein condensates, Phys. Rev. A **69**, 033606 (2004).

[76] S. S. Natu, X. Li, and W. S. Cole, Striped ferronematic ground states in a spin-orbit-coupled $S = 1$ Bose gas, Phys. Rev. A **91**, 023608 (2015).

[77] L. Chen, Y. Zhang, and H. Pu, Spin-Nematic Vortex States in Cold Atoms, Phys. Rev. Lett. **125**, 195303 (2020).

[78] Y. Gao and Y. Cai, Numerical methods for Bogoliubov-de Gennes excitations of Bose-Einstein condensates, J. Comput. Phys. **403**, 109058 (2020).

[79] B. A. Malomed, *Soliton Management in Periodic Systems* (Springer, Berlin, 2006).

[80] W. Liu and Y. Cai, Normalized gradient flow with Lagrange multiplier for computing ground states of Bose-Einstein condensates, SIAM J. Sci. Comput. **43**, B219 (2021).

[81] W. Bao and Y. Cai, Mathematical models and numerical methods for spinor Bose-Einstein condensates, Commun. Comput. Phys. **24**, 899 (2018).